
Article:

Levin, I., Laws, W.J., Wang, D. et al. (2017) Designing pseudocubic perovskites with enhanced nanoscale polarization. Applied Physics Letters , 111 (21). 212902. ISSN: 0003-6951

https://doi.org/10.1063/1.5007700

This is an author produced version of the following article: Appl. Phys. Lett. 111, 212902 (2017), which can be found at: https://doi.org/10.1063/1.5007700

Designing Pseudocubic Perovskites with Enhanced Nanoscale Polarization

I. Levin[1], W. J. Laws[1], D. Wang[2] and I. M. Reaney[2]

[1]Materials Measurement Science Division
National Institute of Standards and Technology
Gaithersburg MD 20899 USA

[2]Department of Materials Engineering
University of Sheffield
Sheffield S1 3JD UK

Abstract

A crystal-chemical framework has been proposed for the design of pseudocubic perovskites with nanoscale ferroelectric order, and its applicability has been demonstrated using a series of representative solid solutions that combined ferroelectric ($K_{0.5}Bi_{0.5}TiO_3$, $BaTiO_3$, $PbTiO_3$) and antiferroelectric (Nd-substituted $BiFeO_3$) end members. The pseudocubic structures obtained in these systems exhibited distortions that were coherent on a scale ranging from sub-nanometer to tens of nanometers but, in all cases, the macroscopic distortion remained unresolvable even if using high-resolution X-ray powder diffraction. Different coherence lengths for the local atomic displacements account for the distinctly different dielectric, ferroelectric, and electromechanical properties exhibited by the samples. The guidelines identified provide a rationale for chemically tuning the coherence length to obtain the desired functional response.

The electromechanical and dielectric properties of perovskite-structured complex metal oxides are enhanced near morphotropic or polymorphic phase boundaries that separate two ferroelectric phases with distinctly oriented spontaneous polarization. The archetype system of this type is lead zirconium titanate [1], the properties in which are amplified at the rhombohedral-tetragonal morphotropic phase boundary (MPB). For decades, the search for commercially viable formulations has focused on such MPB compositions but, recently, a different class of perovskite oxides has emerged that also exhibits technologically attractive functional properties [e.g., 2-11]. These materials are multicomponent (≥4 metal components) solid solutions of distorted end-members but which by powder diffraction appear to have the cubic (pseudocubic) symmetry of an ideal ABO_3 perovskite structure (space group *Pm3m*, lattice parameter $a \approx 4$ Å).

From crystal chemistry considerations, it is expected that competing bonding requirements of different cations that share the same crystallographic sites generate local distortions away from the average cubic arrangement. In some of the known pseudocubic perovskite solid solutions, the distortions are coherent over a scale of only a few nanometers (or less), whereas in others their coherence extends over a longer range but remains weak and, therefore, unresolvable even with high-resolution diffractometers. Examples of the first type of structures can be found in $BaTiO_3$-$BiMO_3$ (M=Sc, $Mg_{½}Ti_{½}$, $Zn_{½}Ti_{½}$) systems [11], which yield dielectric properties of interest for high-energy capacitor applications; and in $Bi_{½}K_{½}TiO_3$-(Bi,Nd)FeO_3 ceramics that generate strong, temperature-stable electromechanical responses [8]. An example of the second type is (K,Bi)(Nb,Fe)O_3, which displays a widely tunable band gap in a long-range but weakly correlated ferroelectric structure [9].

Despite a growing number of reports on pseudocubic perovskites with promising dielectric/electromechanical properties, the general principles for their rational design have not been well articulated. Likewise, the links between the pseudosymmetry (i.e., symmetry that varies with the length scale) of these materials and their functional performance remain uncertain. In this letter, we propose an intuitive crystal-chemical framework that can guide the development of pseudocubic formulations with specific functional responses and illustrate its plausibility using several examples.

As a starting point, we note that the high-temperature cubic phases of classical ABO_3 ferroelectric compounds already exhibit pseudosymmetry because of significant local distortions that can be interpreted as precursors of the lower-temperature ferroelectric states. For example, X-ray absorption fine structure measurements suggest that the cubic phases of $BaTiO_3$ and $PbTiO_3$ feature local rhombohedral-like and tetragonal-like distortions, respectively, which correspond to the symmetries of their ground states [12, 13]. Thus, one approach to obtaining room-temperature pseudocubic phases with large local electric dipoles could involve using chemical substitutions to suppress long-range distortions in such ferroelectric end-members while promoting polar distortions on the local scale.

Crystal-chemical considerations and analyses of the published systems suggests the following key components that are required to stabilize such pseudosymmetric states with synergetic enhancement of the local polarization:

(1) Large A-cations (e.g., Ba, K, Pb);
(2) Smaller A-site (e.g., Bi, Ca, Na) and B-site cations (e.g., Ti, Nb) prone to off-centering;
(3) Non-ferroelectric, “blocking” cations on A and/or B sites (e.g., Ba, K, rare-earth ions, Sc, Mg).

The presence of large A-cations is required to create a "host" framework that contains relatively oversized $[AO_{12}]$ cube-octahedral and $[BO_6]$ octahedral cages so that polar shifts of the smaller A and B species, substituted into these cages, are the primary mechanisms for relieving the A-O and B-O bond tension. The role of small "rattling" ions on both sites is to generate locally correlated electric dipoles; such short-range correlations have been proposed to facilitate reorientation of the local polarization under an applied electric field [14]. Finally, the non-ferroelectric cations are required to disrupt long-range correlations among the ionic displacements, thereby suppressing lattice distortions.

In the present study, we use several representative systems to demonstrate the applicability of these principles. For the end members, we selected tetragonal (space group *P4mm*) ferroelectrics exhibiting distinct c/a ratios and Curie temperatures (T_C): $K_{0.5}Bi_{0.5}TiO_3$ (KBT, c/a≈1.01, T_C≈270 °C), $BaTiO_3$ (BT, c/a≈1.01, T_C≈123 °C), and $PbTiO_3$ (PT, c/a≈1.06, T_C≈495 °C). KBT differs from the two other compounds by the presence of a disordered cation mixture (i.e. K and Bi) on the A-sites. The Goldsmith tolerance factors (t) for KBT, BT, and PT are 1.02, 1.062, and 1.02, respectively. All these compounds reportedly exhibit a pseudocubic state at high temperature [12, 13, 15]. The second component of the solid solutions has been chosen to be a recently developed antiferroelectric $Bi_{0.85}Nd_{0.15}FeO_3$ [16, 17] modified with 3 mol % of $Nd_{2/3}TiO_3$, which hereafter is abbreviated as BNFT. At room temperature, this system (t=0.945) forms the orthorhombic $PbZrO_3$-type structure (space group *Pbam*, unit cell $\sqrt{2}a_c \times 2a_c\sqrt{2} \times 2a_c$) [17]. The addition of $Nd_{2/3}TiO_3$ minimizes electrical conductivity and facilitates densification [18].

In the selected systems, Ba^{2+} (ionic radius [19] R=1.61 Å), Pb^{2+} (R=1.49 Å), and K^+ (R=1.64 Å) are large ions that satisfy criterion 1, while Bi^{3+} (R=1.35 Å) and Ti^{4+} (R=0.604 Å) act as rattling ions on their respective sites. Ba^{2+}, K^+, Nd^{3+} (R=1.27 Å) and a small fraction of the structural A-site vacancies are expected to disrupt ferroelectric correlations among the A-cation displacements (Criterion 3). While Nd exhibits a small ionic radius and, as such, could be displaced off-center, it is known, as other rare-earth cations, to suppress the ferroelectric behavior in compounds like $BaTiO_3$ and $BiFeO_3$ [16, 20]. The Fe^{3+} (R=0.645 Å) ions are non-ferroelectric but support large lattice distortions in the tetragonal $PbTiO_3$-$BiFeO_3$ phase [21, 22], and, thus, may not necessarily act as "blocking" species. While the pseudocubic phase in KBT-BNFT has been reported previously [8], we included it here for consistency and a more detailed characterization of its structure.

Ceramic compositions in the KBT-BFNT, BT-BFNT, and PT-BFNT, systems (including the tetragonal end-members) were prepared with an increasing fraction of the BFNT component until a single cubic phase was obtained at room temperature, as deduced from X-ray powder diffraction patterns. No attempt to delineate the entire cubic phase field has been made in this initial work. All samples were processed using conventional solid-state synthesis. Appropriate amounts of raw powders of K_2CO_3 (A.R.), $BaCO_3$ (A.R), Bi_2O_3, Nd_2O_3 (99.99 %), TiO_2 (<10 ppm P_2O_5), and Fe_2O_3 (A.R) were mixed under acetone using an agate mortar and pestle. After drying, the mixtures were ball-milled in isopropanol using yttria-stabilized zirconia cylinders as a grinding media. The dried powders were calcined at 850 °C. After subsequent ball milling, the powders were pressed into pellets (with PVA added) and heated in air at 1000 °C for 5 h twice with intermediate grinding. Laboratory X-diffraction (XRD) with Cu $K\alpha_1$ radiation was used to confirm phase compositions and to perform variable-temperature measurements of peak broadening. High-resolution XRD patterns were collected at the 11-BM beamline of the Advanced Photon Source (APS) at the Argonne National Laboratory. The local structure was probed using pair distribution functions (PDF) determined from total X-ray scattering as measured at the 11-ID-B beamline of the APS using an incident-beam energy of 86 kV (wavelength 0.143 Å) and a 2-D detector. The samples were loaded in kapton capillaries. The Fit2D software was used to reduce the 2-D diffraction patterns to 1-D intensity traces, which were subsequently converted to PDFs. TEM studies were conducted in a conventional instrument operated at 200 kV. Samples for TEM were prepared either using mechanical polishing followed by ion thinning at T=-100 °C until perforation. The ion-thinned samples were annealed at 500 °C in air to remove residual stresses that could result from mechanical polishing.

X-ray diffraction patterns for the 0.91KBT-0.09BNFT (*t*=1.015 [22]), 0.85BT-0.15BNFT (*t*=1.044), and 0.4PT-0.6BNFT (*t*=0.976) compositions (Fig. S1) could all be accounted for by a single cubic perovskite phase. These concentrations of BNFT are close to the respective minimum values that were required to stabilize the cubic phase; the threshold content scales with the *c*/*a* ratio of the end compound. In all the systems studied here, the distortions remain unresolvable over a relatively broad compositional range (> 10 %), which supports the existence of an extended pseudocubic phase field. Fig. 1 displays traces of the 002 and 110 reflections, which yield narrow, relatively symmetric single peaks without any detectable splitting.

The ability to form a cubic phase is particularly interesting for 0.4PT-0.6BNFT, which can be rewritten as 0.892($Pb_{0.45}Bi_{0.55}Ti_{0.45}Fe_{0.55}O_3$) - 0.108($Nd_{0.945}Fe_{0.833}Ti_{0.167}O_3$). The $Pb_{0.45}Bi_{0.55}Ti_{0.45}Fe_{0.55}O_3$ solid solution is tetragonal with an anomalously large *c*/*a*≈1.17 and T_C≈625 °C [21, 22]. Evidently, substitution of ≈11 mol Ti-doped $NdFeO_3$ is sufficient to suppress this distortion with the resulting diffraction peaks being the narrowest among the three systems (Fig. 1).

The extent of lattice distortions in pseudosymmetric structures can be assessed by following the temperature dependence of peak widths in XRD patterns. Such variable-temperature measurements performed here for the 002 reflection revealed changes attributable to a pseudocubic↔cubic phase transition (Fig. 2). The effects are most pronounced in the KBT-BNFT (Fig. 2a) and PT-BNFT (Fig. 2c) systems, which exhibit significant peak narrowing (on heating) around ≈150 °C and ≈200 °C, respectively; in both cases, these changes are spread over a broad (>200 °C) temperature range. For the (1-*x*)KBT-*x*BNFT solid solutions, the transition occurs at similar temperatures for the three synthesized compositions (x=0.09, 0.15, 0.2). In the PT-BNFT samples, residual stresses introduced during grinding had a dramatic effect on the peak broadening as evident from Fig. 2c; for two other systems, the effects of stresses, while present, are less significant. The BT-BNFT (Fig. 2b) solid solutions exhibit only weak narrowing of the peak on heating and the magnitude of these changes is too small to reliably claim the existence of a transition.

X-ray PDFs determined for the solid-solution samples (Fig. 3) mostly reveal distances that involve the heavy Ba, Nd, Pb, and Bi atoms which dominate X-ray scattering. Fitting a cubic perovskite model to these PDFs yields satisfactory agreement for *r*>10 Å (Fig. S2, Table S1), consistent with the inferences from the Bragg peaks. For *r*<10 Å, however, significant discrepancies are observed, indicative of substantial local distortions on the length scale of at least several perovskite unit cells (Fig. S2, S3). Comparison of the PDFs (Fig. 3) for the solid solutions and their respective end-compounds suggests that the local structures in both KBT-BNFT and BT-BNFT compositions resemble those exhibited by KBT and BT, respectively. The structure of PT-BNFT differs considerably from that of PT over the entire distance range, which is understandable given that this solid solution incorporates a major fraction of BNFT. The PDFs for the 91KBT-9BNFT and KBT samples remain remarkably similar up to at least 20 Å, which suggests that the KBT-like distortions persist on the nanoscale. The discrepancies between the PDFs of BT and 85BT-15BNFT become much more noticeable already beyond 6 Å; therefore, the distortions in this system appear to be limited to a shorter range. For all the systems, the PDFs reveal a short Bi-O distance of ≈2.2 Å, which is typical for Bi^{3+} ions off-centered in oversized A-site cages.

TEM further confirms that the local distortions in the studied structures remain coherent beyond the unit-cell scale (Fig. 4). Dark-field TEM imaging of individual grains in 0.91KBT-0.09BNFT (Fig. 4a) display a mottled contrast suggestive of nanoscale domains 2-5 nm size. For the 0.4PT-0.6BNFT samples, selected-area electron diffraction patterns (inset in Fig. 4b, c) contained *½hhl* (*h, l*=2n+1) superlattice reflections attributable to ordered anti-phase octahedral rotations; ⟨100⟩ diffuse streaks passing through these spots suggest a significant tilting-sign disorder. The occurrence of octahedral rotations is not surprising for this composition, which has a tolerance factor of 0.976; the superlattice peaks remain practically undetectable by XRD, presumably because of the small rotation angles (per simulations, <5 °) and tilting disorder. Dark field imaging using the fundamental reflections (Fig. 4b) highlighted the assemblages of twin-domain variants ≈20 nm thick, which can be attributed to nanoscale distortions caused by polar cation displacements. The traces of these domain walls match those of {110} planes. Concurrently, imaging using the superlattice spots (Fig. 4c) revealed a substructure of another type of twin domains, <20 nm thick, with domain walls parallel to the {001} planes, along with relatively large, irregular-shaped anti-phase domains (≈250 nm) (Fig. S4), presumably associated with octahedral rotations. The domain structure associated with the superlattice reflections is linked to octahedral rotations; the nature of these tilting twin domains resembles that observed in $Na_{½}Bi_{½}TiO_3$ [24]. The distinct ferroelectric and tilting twin domains suggest that the coupling between the ferroelectric and tilting order is weak, which can be one reason for a small lattice distortion.

As reported previously [8], the 91KBT-09BNFT composition exhibits dielectric relaxation and slim *P-E* loops consistent with those of relaxor ferroelectrics. This material generates high, temperature-stable electromechanical strain (*S*), which makes it of interest for practical applications. Both 85BT-15BNFT (doped with 0.2 wt. % Mn to suppress electrical conductivity) and 40PT-60BFNT samples [25] also exhibit dielectric relaxations with broad, frequency-dependent peaks of dielectric permittivity as a function of temperature (Fig. 5 a, b). While the BT-BNFT sample generated the slim *P-E* and *S-E* loops of a relaxor (Fig. 5c), the PT-BNFT ceramic yielded *P-E*/*S-E* loops that are typical for an ordered ferroelectric (Fig. 5d), in contrast to its relaxor-like dielectric properties. This apparent discrepancy between the supposedly inter-related properties in PT-BNFT can be reconciled if the application of a sufficiently large electric field strengthens the coupling between the ferroelectric and tilting distortions, which promotes the long-range ordered ferroelectric state. The observed sensitivity of the structural distortion in this system to residual stresses, which evidently induce a more distorted state, is assumed to be the manifestation of a pseudocubic structure on the verge of a transition to a structure with long-range order. Thus, the application of a mechanical or an electric field triggers this change.

Overall, the properties are controlled by the spatial extent of local structural distortions, which in turn depend on the type and concentrations of the blocking species. For example, a combination of large Ba (A-site) and Sc (B-site) ions in the $BaTiO_3$-$BiScO_3$ solid solutions [26] limit the correlations among the Bi and Ti displacements to only 1-2 perovskite unit cells. In contrast to Sc, the non-ferroelectric Zn cations can form covalent bonds with oxygen and are known to support a large tetragonal distortion in $BiZn_{½}Ti_{½}O_3$ [27, 28]. Therefore, the $BaTiO_3$-$BiZn_{½}Ti_{½}$O3 solid solutions, while also pseudocubic, feature more extended distorted regions [29] than $BaTiO_3$-$BiScO_3$ [26] because Zn ions are less effective disruptors of correlations than Sc. For the presently studied systems, the high concentration of Ba atoms in 85BT-15BNFT more effectively limits the correlations among polar displacements than a significantly lower concentration of K in 91KBT-9BNFT. The absence of large non-ferroelectric A-site cations in the PT-BNFT system yields even greater correlation lengths, which are limited primarily by the Nd cations and, possibly, by octahedral tilting.

Thus, with the first two criteria for stabilizing a pseudocubic structure satisfied, the selection of blocking species and their concentrations can be used to tune material properties. For example, maximum electromechanical strain can be enhanced drastically from a modest value in 85BT-15BNFT to technologically relevant levels in 30BT-70BNF [10], which features a significantly smaller fraction of the blocking Ba and Nd species (here, the concentration of Nd in BNF has been adjusted to 0.02). Distortions that compete with and remain only weakly coupled to ferroelectric ordering (e.g., octahedral tilting) can also disrupt polar correlations, as observed here for PT-BNFT and previously for other PT-based systems [30, 31].

In summary, we propose crystal-chemical guidelines for the design of pseudocubic perovskite solid solutions with nanoscale ferroelectric order. These ideas have been used to generate pseudocubic phases in several representative systems, utilizing a single antiferroelectric in combination with three well-known tetragonal end members. The spatial extent of polar ordering in the obtained structures varied from sub-nanometer to tens of nanometers, which resulted in markedly different ferroelectric/electromechanical properties. The chemistry-structure-properties relations derived in this study provide a basis for the development of multicomponent ferroelectric perovskites with optimized and potentially exploitable functional responses.

Supplementary Material

The supplementary material provides additional results of sample characterization.

Acknowledgements

This research used resources of the Advanced Photon Source, a U.S. Department of Energy (DOE) Office of Science User Facility operated for the DOE Office of Science by Argonne National Laboratory under Contract No. DE-AC02-06CH11357.

References

1. B. Jaffe, W. R. Cooke Jr and H. Jaffe, Piezoelectric Ceramics, Academic Press, ISBN 10: 0124332617
2. H. Ogihara, C. A. Randall, S. Trolier-McKinstry, J. Am. Ceram. Soc., 92 [8] 1719 (2009)
3. B. Xiong, H. Hao, S. J. Zhang, H. X. Liu, M. H. Cao, J. Am. Ceram. Soc., 94 [10] 3412 (2011)
4. N. Raengthon, T. Sebastian, D. Cumming, I. M. Reaney, D. P. Cann, J. Am.Ceram. Soc., 95 [11] 3554 (2012)
5. R. A. Malik, A. Hussain, A. Maqbool, A. Zaman, C-W Ahn, J. U. Rahman, W-J. Kim, M-H. Kim, J. Am. Ceram. Soc., 98 [12] 3842 (2015)
6. Y. X. Wei, C. Q. Jin, Y. M. Zeng, X. T. Wang, G. Xu, X. L. Wang, Materials, 8 [12] 8355 (2015)
7. J. G. Hao, Z. J. Xu, R. Q. Chu, W. Li, J. Du, J. Mater. Sci., 50 [15] 5328 (2015)
8. A. Khesro, D. Wang, F. Hussain, D. C. Sinclair, A. Feteira, I. M. Reaney, Appl. Phys. Lett., 109 (14) 142907 (2016)
9. C. Pascual-Gonzalez, G. Schileo, S. Murakami, A. Khesro, D. Wang, I. M. Reaney, A. Feteira, Appl. Phys. Lett., 110, 172902 (2017)
10. D. Wang, A. Khesro, S. Murakami, A. Feteira, Q. Zhao, I. M. Reaney, J. Eur. Ceram. Soc., 47 [4], 1857 (2017)
11. M. A. Beuerlein, N. Kumar, T-M. Usher, H. J. Brown-Shaklee, N. Raengthon, I. M. Reaney, D. P. Cann, J. L. Jones, and G. L. Brennecka, J. Am. Ceram. Soc., 2849 (2016)
12. B. Ravel, N. Sicron, Y. Yacoby, E. A. Stern, F. Dogan, J. J. Rehr, Ferroelectrics, 164 [1], 265-277 (2011)
13. B. Ravel, E. A. Stern, R. I. Vedrinskii, V. Kraizman, Ferroelectrics, 206 [1], 407 (1998)
14. V. Krayzman, I. Levin, J. C. Woicik, F. Bridges, Appl. Phys. Lett., 107, 192903 (2015)
15. V. V. Ivanova, A. G. Kapyshev, Yu.N. Venevtsev, G. S. Zhdanov, Bull. Acad. Sci. USSR Phys. Ser. 26, 358 (1962)
16. S. Karimi, I. M. Reaney, Y. Han, J. Pokorny, I. Sterianou, J. Mater. Sci., 44, 5102 (2009)
17. S. Karimi, I. M. Reaney, I. Levin, and I. Sterianou, Appl. Phys. Lett., 94, 112903 (2009)
18. K. Kalantari, I. Sterianou, S. Karimi, M. C. Ferrarelli, S. Miao, D. C. Sinclair, I. M. Reaney, Adv. Funct. Mater., 21 [19], 3737 (2011)
19. R. D. Shannon, Acta Cryst., A32, 751 (1976)
20. Z. Yao, H. Liu, Y. Liu, Z. Wu, Z. Shen, Y. Liu, M. Cao, Mater. Chem. Phys., 109, 475 (2008)
21. S. Bhattacharjee, S. Tripathi, D. Pandey, Appl. Phys. Lett., 91 [4], 042903 (2007)
22. I. Levin, V. Krayzman, M. G. Tucker, J. C. Woicik, Appl. Phys. Lett., 104 [24], 242913 (2014)
23. For solid solutions, the tolerance factor (*t*) was calculated assuming average ionic radii for the A and B sites.
25. I. Levin and I. M. Reaney, Adv. Funct. Mater., 22 [16], 3445 (2012)
26. Pellets used for the dielectric/piezoelectric property measurements have been sintered at 1150 °C – 1200 °C (3 h) and 1020 °C –1060 °C (2 h) for the 0.85BT-0.15BNFT and 0.4PT-0.6BNFT compositions, respectively.
27. I. Levin, V. Krayzman, J. C. Woicik, F. Bridges, S. E. Sterbinsky, T. M. Usher, D. Torrejon, Phys. Rev. B., 93 [10] 104106 (2016)
28. M. R. Suchomel, P. K. Davies, Appl. Phys. Lett., 86 [26] 262905 (2005)

29. I. Grinberg, M. R. Suchomel, W. Dmowski, S. E. Mason, H. Wu, P. K. Davies, A. M. Rappe, Phys. Rev. Lett., 98 [10] 107601 (2007)
30. D. Hou, T. M. Usher, H. H. Zhou, N. Raengthon, N. Triamnak, D. P. Cann, J. S. Forrester, J. L. Jones, J. Appl. Phys. 122 [6], 8823 (2017)
31. D. I. Woodward, I. M Reaney, J. Phys. Cond. Matter, 16 [49] (2004)
32. C. J. Stringer, R. E. Eitel, T. R. Shrout, C. A. Randall, I. M. Reaney, J. Appl. Phys. 97 (2), 024101 (2005)

Figure Captions:

Fig. 1: Magnified view of the (a) 002 and (b) 110 diffraction peaks recorded using a high-resolution diffractometer and synchrotron radiation in 91KBT-9BNFT (red), 85BT-15BNFT (blue), and 40PT-60BNFT (green). The peaks have been shifted and re-scaled to facilitate comparison of their widths.

Fig. 2: Temperature dependence of the full-width-at-half-maximum (FWHM) for the 002 diffraction peak for (a) 85BT-15BNFT, (b) 91KBT-9BNFT, and (c) 40PT-60BNFT. In (c), the dependence is shown before (left axis) and after (right axis) the post-grinding annealing. For two other samples, the effect of this annealing was relatively insignificant. The error bars reflect a single standard deviation associated with the peak fitting.

Fig. 3: Experimental pair-distribution functions derived from total X-ray scattering for (a) KBT (red) and 91BT-9BNFT (blue), (b) BT (red) and 85BT-15BNFT (blue), and (c) PT (red) and 40PT-60BNFT (blue). The top and bottom plots for each composition emphasize the local- and longer-range distributions of interatomic distances, respectively.

Fig. 4: Dark field TEM images of a single grain in (a) 91KBT-9BNFT, recorded with the 110-type reflection strongly excited near the $\langle 111 \rangle$ zone-axis orientation, and in (b-c) 40PT-60BNFT, recorded with 311 (b) and ½ 311-type (c) reflections strongly excited near the $\langle 311 \rangle$ zone-axis. The inset in (a) shows a magnified view of the contrast attributed to a nanoscale domain texture. The inset in (b-c) shows a selected area electron diffraction pattern from the imaged crystallite with the ½ 311 reflections indicated using arrows. The traces of the domain walls in (b-c) are indicated using dashed lines.

Fig. 5: Temperature dependence of the dielectric constant (solid lines) and losses (dashed lines) as a function of frequency in (a) 85BT-15BNFT and (b) 40PT-60BNFT; black – 1kHz, red – 10 kHz, green – 100 kHz, blue – 250 kHz. *P-E* (solid line) and *S-E* (dashed line) loops for (c) 85BT-15BNFT and (d) 40PT-60BNFT.

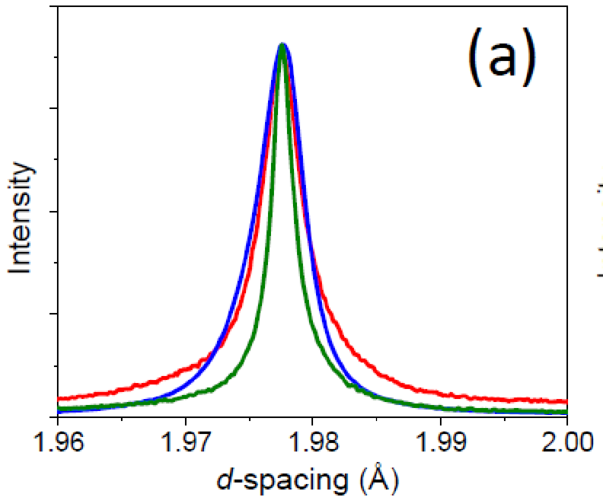
(a)
Intensity
1.96
1.97
1.98
1.99
2.00
d-spacing (Å)
(b)
Intensity
2.76
2.78
2.80
2.82
d-spacing (Å)

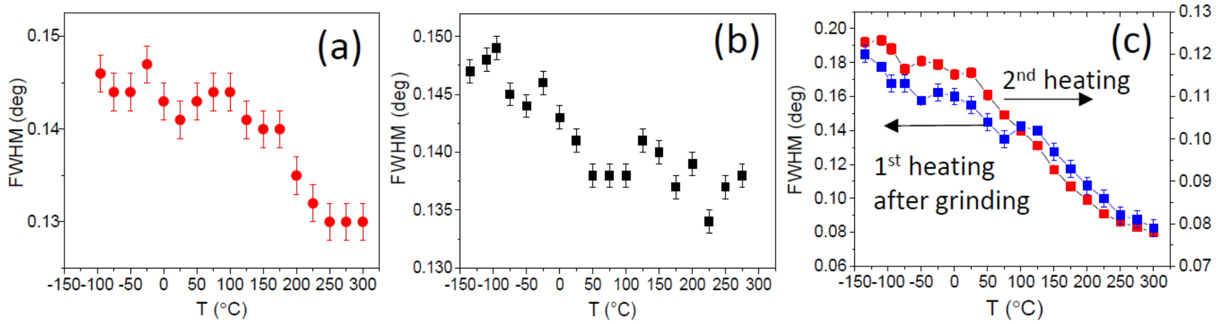
(a)
FWHM (deg)
0.15
0.14
0.13
-150-100 -50 0 50 100 150 200 250 300
T (°C)
(b)
FWHM (deg)
0.150
0.145
0.140
0.135
0.130
-150-100 -50 0 50 100 150 200 250 300
T (°C)
(c)
FWHM (deg)
0.20
0.18
0.16
0.14
0.12
0.10
0.08
0.06
0.13
0.12
0.11
0.10
0.09
0.08
0.07
2nd heating
1st heating after grinding
-150-100 -50 0 50 100 150 200 250 300
T (°C)

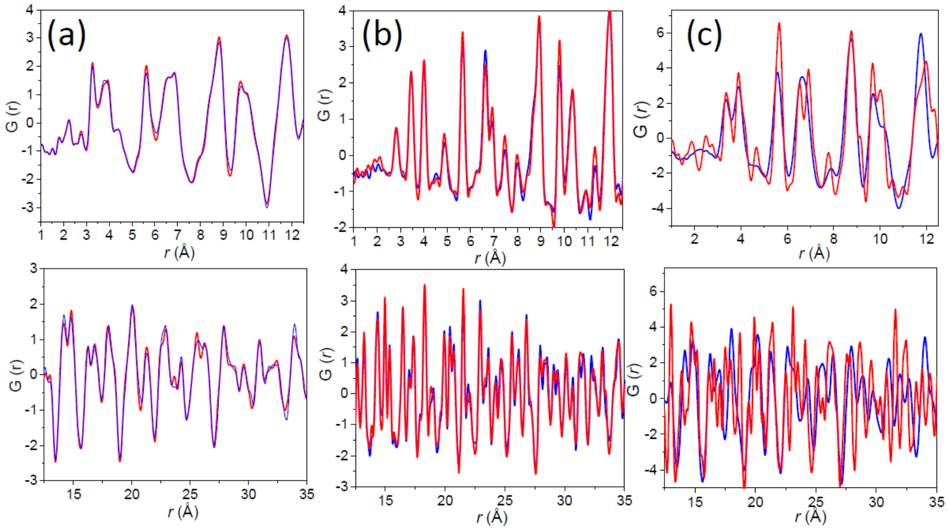
(a)
G (r)
r (Å)
(b)
G (r)
r (Å)
(c)
G (r)
r (Å)
15
20
25
30
35

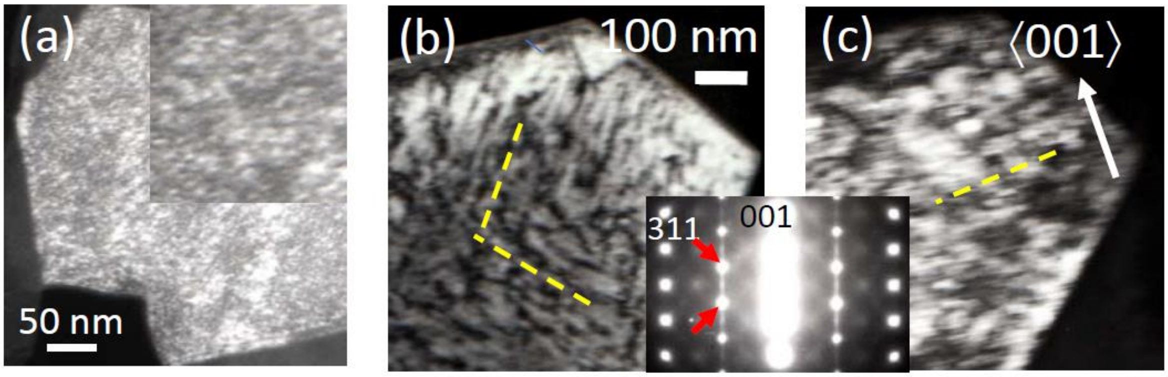
(a)
50 nm
(b)
100 nm
311
001
(c)
⟨001⟩

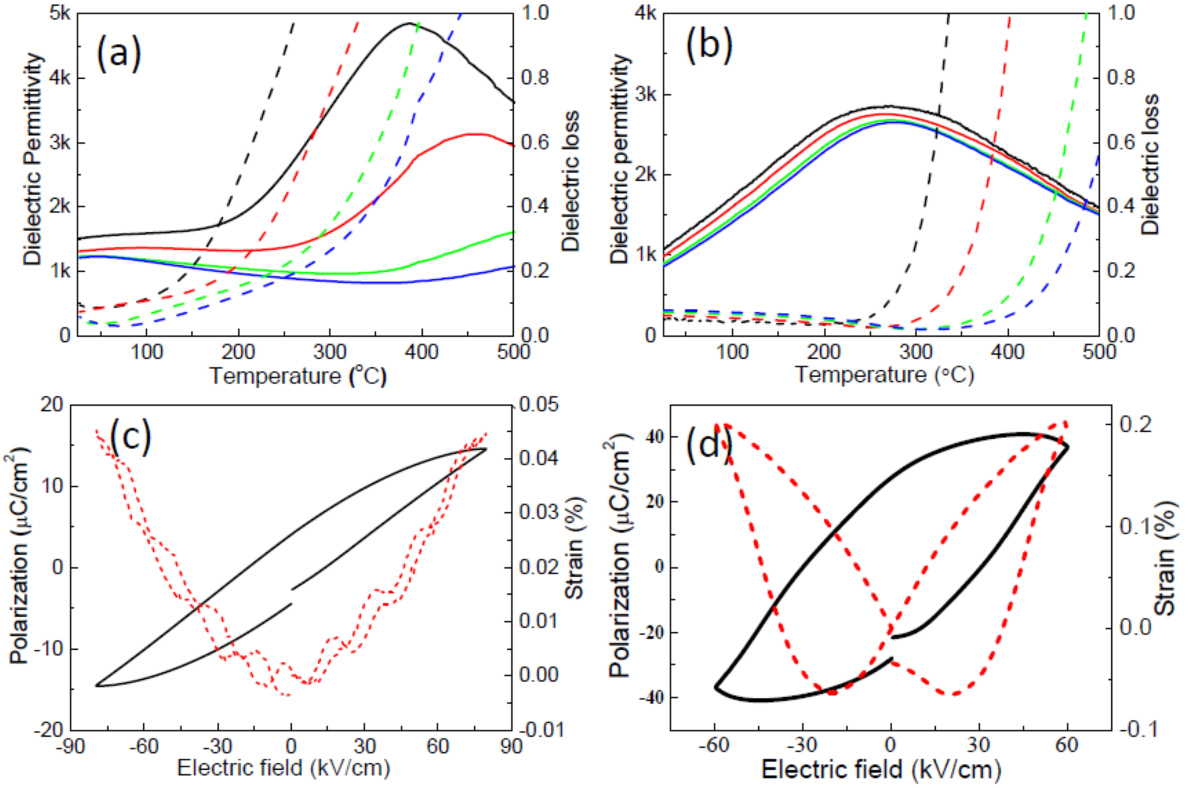
(a)
Dielectric Permittivity
Dielectric loss
5k
4k
3k
2k
1k
0
1.0
0.8
0.6
0.4
0.2
0.0
100
200
300
400
500
Temperature (°C)
(b)
Dielectric permittivity
Dielectric loss
4k
3k
2k
1k
0
Temperature (°C)
(c)
Polarization (μC/cm²)
Strain (%)
20
10
0
-10
-20
0.05
0.04
0.03
0.02
0.01
0.00
-0.01
-90
-60
-30
0
30
60
90
Electric field (kV/cm)
(d)
Polarization (μC/cm²)
Strain (%)
40
20
0
-20
-40
0.2
0.1
0.0
-0.1
-60
-30
0
30
60
Electric field (kV/cm)